



Defective g-C₃N₄/covalent organic framework van der Waals heterojunction toward highly efficient S-scheme CO₂ photoreduction

Jiangpeng Wang^{a,1}, Yue Yu^{a,1}, Jiayi Cui^a, Xinran Li^a, Yilin Zhang^a, Chao Wang^a,
Xuelian Yu^{a,b,*}, Jinhua Ye^{b,*}

^a Beijing Key Laboratory of Materials Utilization of Nonmetallic Minerals and Solid Wastes, National Laboratory of Mineral Materials, School of Materials Science and Technology, China University of Geosciences, Beijing 100083, PR China

^b International Center of Materials Nanoarchitectonics (WPI-MANA), National Institute for Materials Science (NIMS), 1-1 Namiki, Tsukuba, Ibaraki 305-0044, Japan

ARTICLE INFO

Keywords:

VdW heterojunction
CO₂ reduction
S-scheme heterojunction
Nitrogen vacancy
Covalent organic frameworks

ABSTRACT

In this work, a novel van der Waals (vdW) heterojunction composite combining g-C₃N₄ with nitrogen vacancies and Tp-Tta COF manifests effective interface contact area and excellent photocatalytic CO₂ reduction performance. First-principles density functional theory calculation and experimental results suggest that the presence of nitrogen vacancies in g-C₃N₄ can widen the Fermi level gap between C₃N₄ (NH) and Tp-Tta COF, promoting the recombination of invalid photogenerated carriers through S-scheme pathway. Benefitted from the accelerated transfer of photogenerated charges at the vdW heterostructure interface, the deactivation of oxygen vacancies in C₃N₄ (NH)/COF is prevented and much higher photocatalytic activity and stability are obtained. The efficient electron transfer and the affinity of Tp-Tta for CO₂ are beneficial to the enhanced CO selectivity. This work provides insights for the design of S-scheme heterojunction photocatalyst for CO₂ reduction.

1. Introduction

The depletion of carbon-emitting fossil fuels and increasing emission of greenhouse gas (CO₂) have caused emerging global energy and environmental crises [1,2]. Using the abundant and free sunlight as energy source, photocatalytic CO₂ reduction has been considered as a potential strategy to concurrently solve the environmental and energy issues [3–6]. To this end, much researches have been focused on the intensive exploration of photocatalysts with low cost and high durability for enhanced solar-to-fuels energy conversion efficiency [7–9]. Compared to mono-component photocatalysts, building heterostructures has attracted great interest because it can boost the separation of photogenerated carriers via electronic band association, simultaneously coupling respective advantages of each components [10]. Especially, van der Waals (vdW) heterostructure can break the limitation of lattice matching for epitaxial growth, which allows unprecedented flexibility and compatibility for new device [11,12]. Graphitic carbon nitride (g-C₃N₄), with a two-dimensional (2D) layered structure, provides an ideal platform for the construction of vdW heterojunctions

by virtue of its appropriate bandgap, mild synthesis process and good stability [13]. To overcome poor binding of CO₂ to catalysts and decrease high energy involved in CO₂ activation, further construction of g-C₃N₄ based vdW heterostructures with ideal interface contact is urgently recommended.

Covalent organic frameworks (COFs), a new class of 2D materials with fascinating structural tunability, have shown potential application in various fields, such as catalysis, gas storage, and optoelectronics [14]. In particular, imine-linked COFs exhibit not only excellent ability to absorb CO₂ molecules but also efficient electron mobility through the delocalization of p-electrons [15,16]. Taking together with the excellent feature and staggered band configuration of both imine-linked COFs and g-C₃N₄, facile preparation of 2D/2D vdW g-C₃N₄/COF heterojunction will be of great importance for the construction of non-metal photocatalysts for CO₂ reduction. Compared to ¹D–²D and ⁰D–²D heterostructures, this face-to-face heterostructure will possess significant advantages of improved interface contact area and accelerated charge transfer rate [17]. Furthermore, among different heterojunctions, S-scheme heterojunction comprising reduction photocatalyst with more

* Corresponding authors at: International Center of Materials Nanoarchitectonics (WPI-MANA), National Institute for Materials Science (NIMS), 1-1 Namiki, Tsukuba, Ibaraki 305-0044, Japan.

E-mail addresses: xlyu@cugb.edu.cn (X. Yu), jinhua.YE@nims.go.jp (J. Ye).

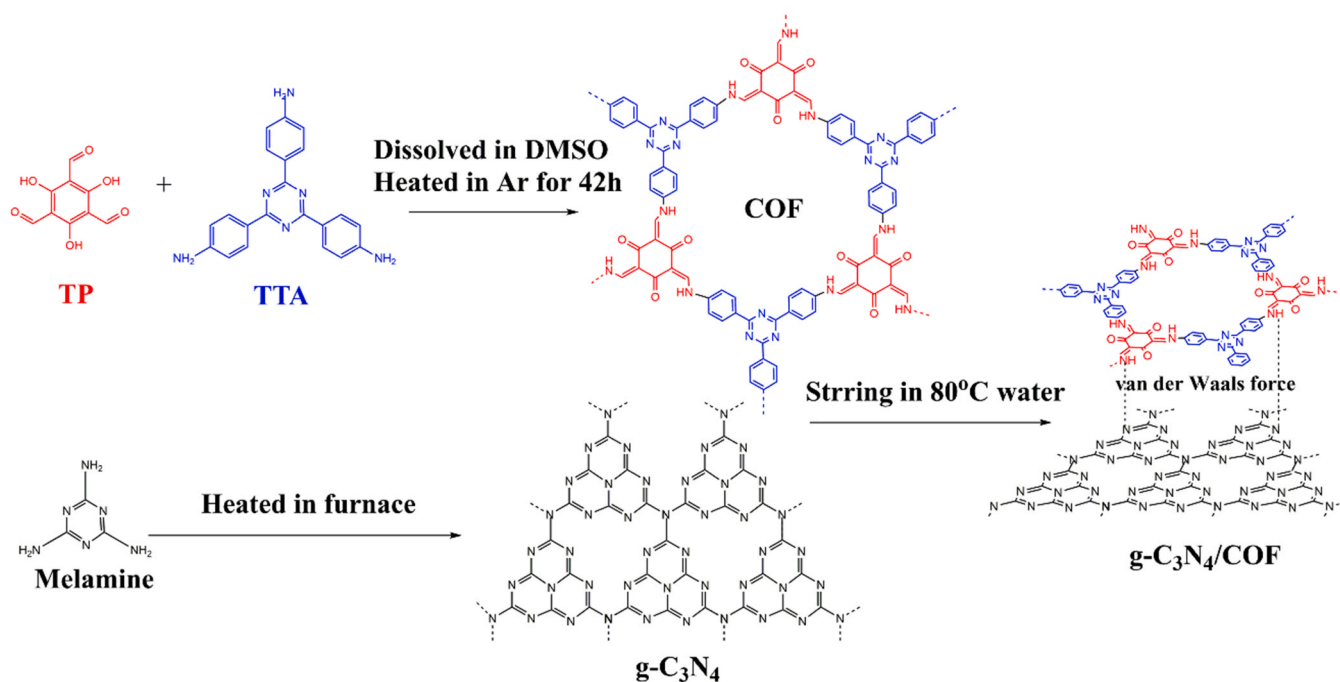
¹ These authors contribute equally to this work.

<https://doi.org/10.1016/j.apcatb.2021.120814>

Received 19 August 2021; Received in revised form 30 September 2021; Accepted 9 October 2021

Available online 13 October 2021

0926-3373/© 2021 Elsevier B.V. All rights reserved.



Scheme 1. Schematic illustration for the preparation of g-C₃N₄/COF vdW heterojunction.

negative conduction band and oxidation photocatalyst with more positive valence band is attractive for preserving charge carriers with maximal redox abilities [18]. Despite great achievements have been made in understanding the charge-transfer routes [19], the efficiency of S-scheme heterojunction for CO₂ photoreduction is still unsatisfactory due to the sluggish reaction dynamics.

The Fermi level gap between reduction and oxidation photocatalyst is endowed as the driving force toward charge-transfer process. Defect engineering can be an effective way to adjust the Fermi level of a semiconductor [20–22]. Especially, recent reports revealed that exfoliating bulk g-C₃N₄ into ultrathin nanosheets would be beneficial to both the exposure of active sites and optimization of electronic structure [23]. Thereby, rational interface regulation based on defective g-C₃N₄ is essential to tailor its electronic structure to improve ultimate photocatalytic performance of g-C₃N₄ based S-scheme heterojunction.

Keeping these in mind, we construct 2D/2D heterojunction photocatalysts coupling defective C₃N₄ nanosheets (C₃N₄ (NH)) with Tp-Tta COF through simple evaporation induced self-assembly method. The C₃N₄ (NH)/COF S-scheme heterojunction with appropriate nitrogen vacancies and strong internal electric field exhibits a stable and highly selective CO (90.4%) generation rate of 11.25 μmol/h under visible light irradiation, which is 45-fold and 15-fold higher than that of g-C₃N₄ and g-C₃N₄/COF, respectively. The strong electronic coupling between defective g-C₃N₄ and Tp-Tta COF connected by the vdW force is confirmed by density function theory calculations and electron paramagnetic resonance analysis. This non-metal heterostructures are expected to serve as a new design protocol for highly efficient photocatalysts.

2. Experimental section

2.1. Synthesis of Tp-Tta COF

4,4',4''-(1,3,5-triazine-2,4,6-triyl) trianiline (Tta, 0.07 mmol) and 1,3,5-Triformylphloroglucinol (Tp, 0.13 mmol) were added in 5 mL DMSO. Then, the mixture was heated and stirred at 120 °C for 42 h under Ar atmosphere. After cooling down, the precipitant was washed thoroughly with methanol. The product was dried at 70 °C for 5 h under

vacuum.

2.2. Synthesis of g-C₃N₄ and g-C₃N₄ (NH)

The g-C₃N₄ was fabricated by annealing 1.5 g melamine in a muffle furnace at 550 °C for 4 h. For g-C₃N₄ (NH), the melamine was annealed in a tube furnace under 10% H₂ and 90% Ar with a flow rate of 10 mL min⁻¹ at 550 °C for 4 h. The use of hydrogen-containing atmosphere can not only facilitate the exfoliation of g-C₃N₄ into ultrathin nanosheets, but also create additional nitrogen vacancies due to the substitution of nitrogen atoms by atomic H [24]. The product was grounded to obtain powder sample for further use.

2.3. Preparation of g-C₃N₄/COF and g-C₃N₄ (NH)/COF composite photocatalyst

An appropriate weight ratio of g-C₃N₄ and Tp-Tta COF was mixed in a certain amount of water. The suspension was ultrasonicated for 1 h and then stirred and heated at 80 °C until all of the solvent was evaporated. The weight percentage of Tp-Tta COF with respect to g-C₃N₄ was varied in the range of 0.5–5 wt%. The g-C₃N₄ (NH)/COF was also obtained using similar method by replacing g-C₃N₄ with g-C₃N₄ (NH).

2.4. Materials characterization

X-ray diffraction (XRD) patterns of samples were collected with a powder X-ray diffractometer (Cu Kα radiation source, X'pert powder, Netherlands). The morphologies were characterized with transmission electron microscope (TEM, ARM-200 F, JEOL Co., Japan). Surface areas were recorded using a BEL SORPmini II (BEL Japan INC., Japan). X-ray photoelectron spectroscopy (XPS) measurements were conducted on XPS instrument (Escalab 250, Thermo SCIENTIFIC, America). The in-situ FTIR measurements were carried out on a JASCO FTIR 6300 spectrometer under CO₂ or Ar atmosphere with a homemade chamber. Nuclear magnetic resonance (NMR) experiments were performed on Bruker AVANCE III 600 spectrometer at a resonance frequency of 600.1 MHz and 150.9 MHz, respectively.

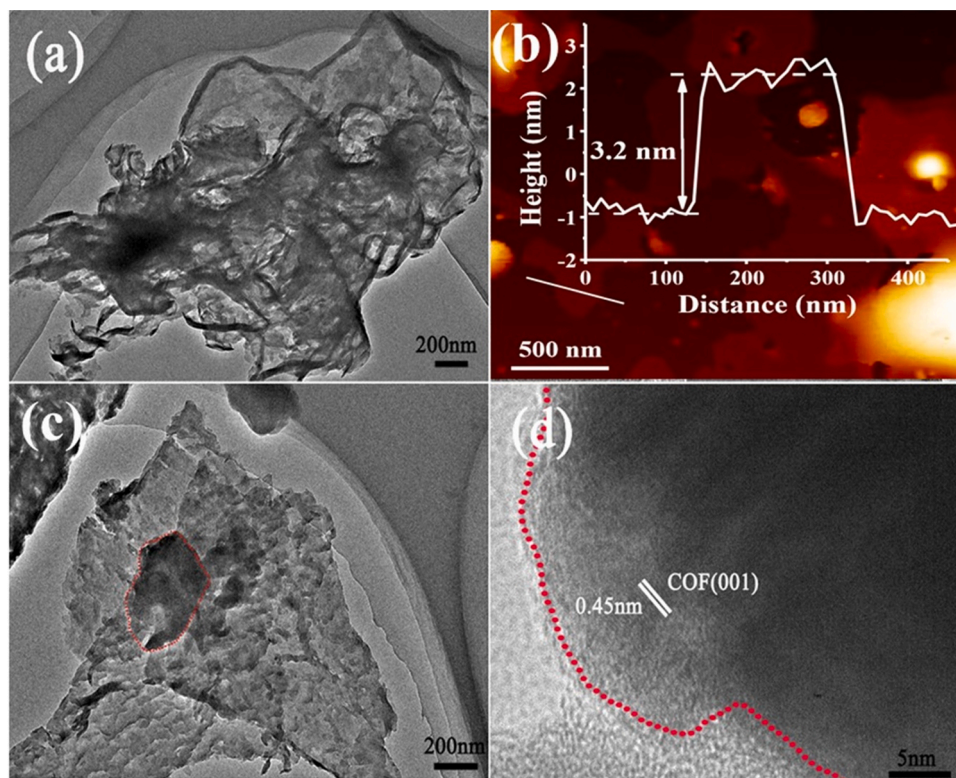


Fig. 1. (a) TEM image of g-C₃N₄ (NH), (b) AFM image of g-C₃N₄ (NH), (c) TEM image of g-C₃N₄ (NH)/COF, (d) HRTEM image of g-C₃N₄ (NH)/COF.

2.5. Photocatalytic CO₂ reduction test

20 mg photocatalyst, 15 mg 2, 2-bipyridine (bpy), and 1 μmol CoCl₂ were dispersed in acetonitrile, deionized water and triethanolamine. After evacuation, the system was injected with CO₂. The light source was a 300 W Xe lamp with water filter and $\lambda > 400$ nm cutoff filter. The gas products, including CO and H₂, were measured by gas chromatography equipped with a thermal conductivity detector (TCD) and a flame ionization detector (FID).

2.6. Photoelectrochemical measurement

The photoelectrochemical properties were investigated in a three-electrode cell by using an electrochemical station (CHI 660E). The catalyst coated ITO glass, Ag/AgCl and Pt were used as the working, reference and counter electrode, respectively. A 300 W Xe arc lamp equipped with cutoff filter ($\lambda > 400$ nm) was utilized as a light source. Electrochemical impedance spectroscopy (EIS) was recorded under a potential of -0.6 V vs Ag/AgCl in the range of 0.1 MHz–0.1 Hz.

2.7. Theoretical calculation

The C₃N₄ with nitrogen vacancies and Tp-Tta surfaces were been built, where the vacuum space along the z direction was set to 18 Å to avoid interaction between neighboring images. All atoms were relaxed adequately. The first principles calculations in the framework of density functional theory were based on the Cambridge Sequential Total Energy Package known as CASTEP [25]. The exchange-correlation functional under the generalized gradient approximation (GGA) with norm-conserving pseudopotentials and Perdew-Burke-Ernzerh of functional was used to describe the electron-electron interaction [26,27]. An energy cutoff of 750 eV and a k-point sampling set of $5 \times 5 \times 1$ were used to be converged. Energy tolerance of 5.0×10^{-7} eV per atom, force tolerance of 0.01 eV Å⁻¹ and maximum displacement of 5.0×10^{-4} Å were considered.

3. Results and discussion

3.1. Characterization of g-C₃N₄ (NH)/COF vdW heterojunction

The fabrication procedure for composite photocatalyst is illustrated in Scheme 1. The reaction and enol to keto tautomerism between Tp and Tta in DMSO gave rise to Tp-Tta COF. Then as-obtained Tp-Tta COF and g-C₃N₄ were sonicated in ethanol solution. After evaporation, Tp-Tta COF nanosheets were assembled on surface of g-C₃N₄ to form the g-C₃N₄/COF vdW heterojunction.

The XRD patterns of g-C₃N₄, g-C₃N₄ (NH), and g-C₃N₄ (NH)/COF are presented in Fig. s1a. For g-C₃N₄, the two peaks at 13.1° and 27.1° are corresponding to (100) in-plane structural packing and (002) interplanar stacking of the conjugated aromatic system, respectively [28]. Under hydrogen atmosphere, the stronger intensity of diffraction peaks in g-C₃N₄ (NH) indicate the improved crystallinity. Moreover, the shift of (002) diffraction peak from 27.1° to 27.6° hints the decreased interplanar distance in g-C₃N₄ (NH). The XRD pattern of pure Tp-Tta COF is shown in Fig. s2. The peak at 2θ value of 5.8° can be indexed to the (100) plane reflection [29]. For g-C₃N₄ (NH)/COF, only the characteristic peaks of g-C₃N₄ (NH) appear due to the relatively low loading content and good dispersion of Tp-Tta COF on g-C₃N₄ (NH) surface. Raman spectra (Fig. s3) show the stretch vibration of C≡N at 2170 cm⁻¹ for g-C₃N₄ (NH) and g-C₃N₄ (NH)/COF. The FTIR spectra of Tp-Tta COF, g-C₃N₄ (NH) and g-C₃N₄ (NH)/COF heterostructure were shown in Fig. s1b. For Tp-Tta COF, the peak at 1622 cm⁻¹ is assigned to stretching frequency of C=O, which appears as a result of enol to keto tautomerism. The strong peak at 1574 cm⁻¹ can be assigned to C=C bond [30]. For g-C₃N₄ (NH), the absorption band at 803 cm⁻¹ corresponds to the breathing mode of triazine units. Absorption bands in the range of 1000–1700 cm⁻¹ correspond to the aromatic C–N and C=N vibrations [31]. The broad band in the range of 3000–3500 cm⁻¹ can be assigned to NH₂ groups and adsorbed water [32]. The bonding state was further confirmed by ¹³C NMR spectra. The Tp-Tta COF displays the characteristic resonance signal at 184.6 ppm assignable to the C=O carbon

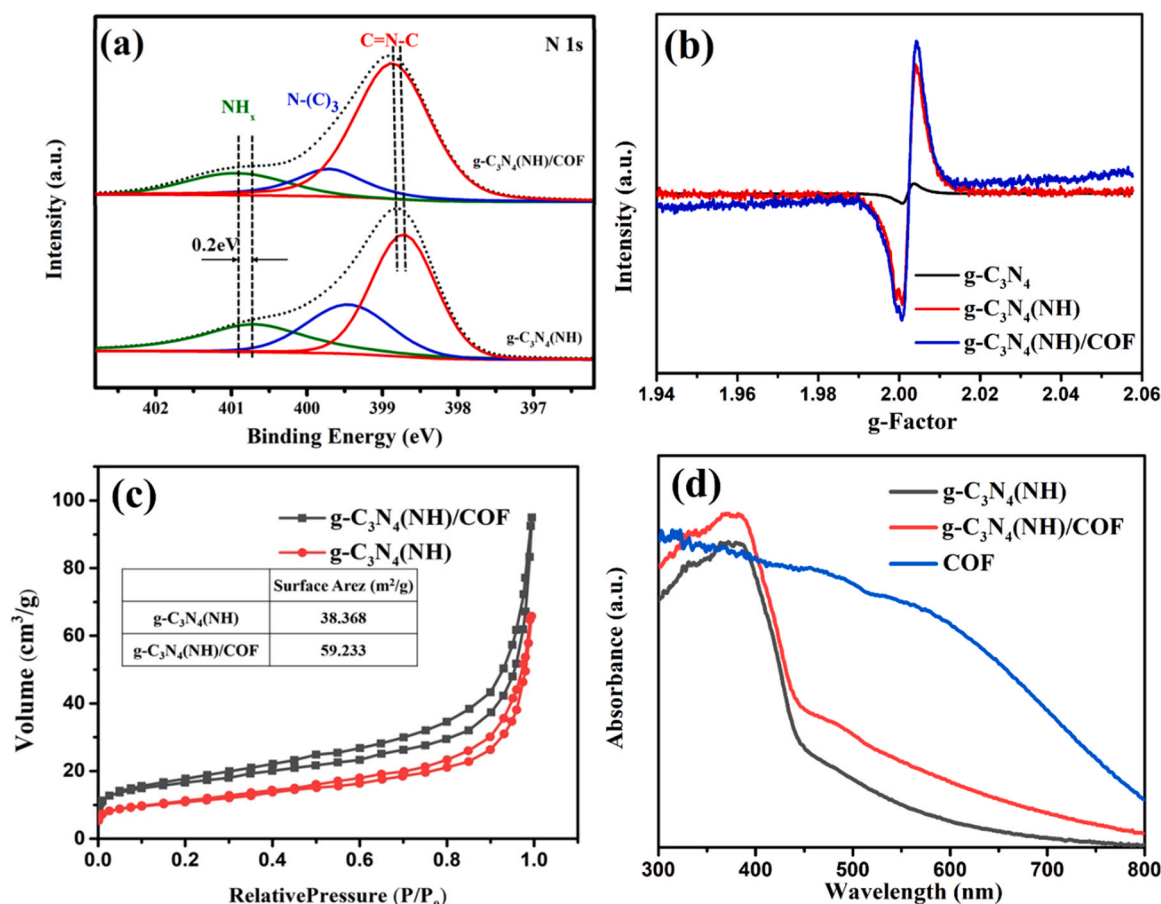


Fig. 2. (a) High-resolution XPS spectra of N 1s in g-C₃N₄ (NH), g-C₃N₄ (NH)/COF. (b) ESR spectra of g-C₃N₄, g-C₃N₄ (NH) g-C₃N₄ (NH)/COF. (c) N₂ physisorption isotherms of g-C₃N₄ (NH) and g-C₃N₄ (NH)/COF. (d) UV-vis spectra of g-C₃N₄ (NH), Tp-Tta COF and g-C₃N₄ (NH)/COF.

(Fig. S1c and S1d), indicating the enol-keto transformation into the respectively stable COFs. Besides, the molecular structure of the building units remains intact during Tp-Tta COFs formation [33]. The signals in g-C₃N₄ (NH) can be assigned to C₂N-NH_x (164.1 ppm) and C₃N (155.9 ppm), respectively [34]. In g-C₃N₄/COF, the coexistence of signals from g-C₃N₄ (NH) and Tp-Tta COF further supports successful preparation of heterostructure.

The surface morphology of the samples was investigated by TEM and AFM analysis. Compared to the thick and agglomerated TEM image of g-C₃N₄ (Fig. S4), the g-C₃N₄ (NH) sheets are more transparent and flat (Fig. 1a). The AFM image in Fig. 1b shows the thickness of g-C₃N₄ (NH) is approximately 3.2 nm. This is induced by the reduced concentration of heptazine ring under hydrogen atmosphere and these ultrathin nanosheets are expected to act as ideal metal-free scaffold for assembling heterostructures. Meanwhile, Tp-Tta COF sheets with several hundreds of nanometers are observed in Fig. S5, indicating their typical 2D structure. Significantly, in g-C₃N₄ (NH)/COF, these nanosheets are uniformly distributed on the surface of g-C₃N₄ (NH) (Fig. 1c). In the HRTEM image (Fig. 1d), the lattice fringe of 0.45 nm is attributed to the (001) facet of Tp-Tta COF, while the lower amorphous layer is ascribed to the g-C₃N₄ (NH) substrate. The intimate interface will facilitate charge separation in the photocatalytic process. All of the above results prove that the Tp-Tta COF can be easily deposited onto g-C₃N₄ (NH) nanosheet to form the g-C₃N₄ (NH)/COF vdW heterostructure through π - π interaction.

X-ray photoelectron spectroscopy (XPS) and electron paramagnetic resonance (EPR) analyses were carried out to investigate the electronic structure in g-C₃N₄ (NH)/COF. The survey results of the XPS spectra in Fig. S6 suggest the existence of C, N and O elements in g-C₃N₄ (NH), Tp-

Tta COF and g-C₃N₄ (NH)/COF. The atomic ratio of C:N calculated by XPS for g-C₃N₄ (NH) is 0.88, implying the release of nitrogen species under hydrogen atmosphere in g-C₃N₄ (NH). Specifically, the N 1s spectrum of g-C₃N₄ (NH) and g-C₃N₄ (NH)/COF shown in Fig. 2a can be deconvoluted into three peaks assigned to C=N-C, N-(C)₃ and N-H_x bonds, respectively. The ratio of the peak area of C=N-C/N-(C)₃ decreases from 2.96 (g-C₃N₄) (Fig. S7) to 2.18 (g-C₃N₄ (NH)), suggesting that the loss of nitrogen occurs at the two-coordinated sites [35]. Moreover, it is obvious that the binding energies of N 1s bond is shifted towards higher binding energy in g-C₃N₄ (NH)/COF, confirming the electron transfer from g-C₃N₄ (NH) to Tp-Tta COF after their coupling. All the above results prove the intense interaction between g-C₃N₄ (NH) and Tp-Tta COF in g-C₃N₄ (NH)/COF vdW heterojunction. The defective structure in the framework was further revealed by the EPR spectroscopy shown in Fig. 2b. The signal at g value of 2.002 arises from unpaired electrons on the carbon atoms of the aromatic rings [36]. Comparably, the much stronger signal of g-C₃N₄ (NH) than that of g-C₃N₄ illustrates the generation of rich nitrogen vacancies in porous nanosheets, which is consistent with the XPS results. It should be pointed out that the ESR signal in g-C₃N₄ (NH)/COF is almost unchanged as that in g-C₃N₄ (NH), indicating the potential modulation and stabilization of unpaired electrons within big π -conjugated aromatic rings in g-C₃N₄ (NH)/COF.

The specific surface areas of g-C₃N₄ (NH) and g-C₃N₄ (NH)/COF were demonstrated by N₂ physisorption test. As shown in Fig. 2c, the specific surface area of g-C₃N₄ (NH)/COF (59.233 m²/g) is slightly larger than that of g-C₃N₄ (NH) (38.368 m²/g). UV-vis spectra were recorded to study the optical properties of prepared samples. As shown in Fig. 2d, g-C₃N₄ (NH) sample displays visible light absorption band below

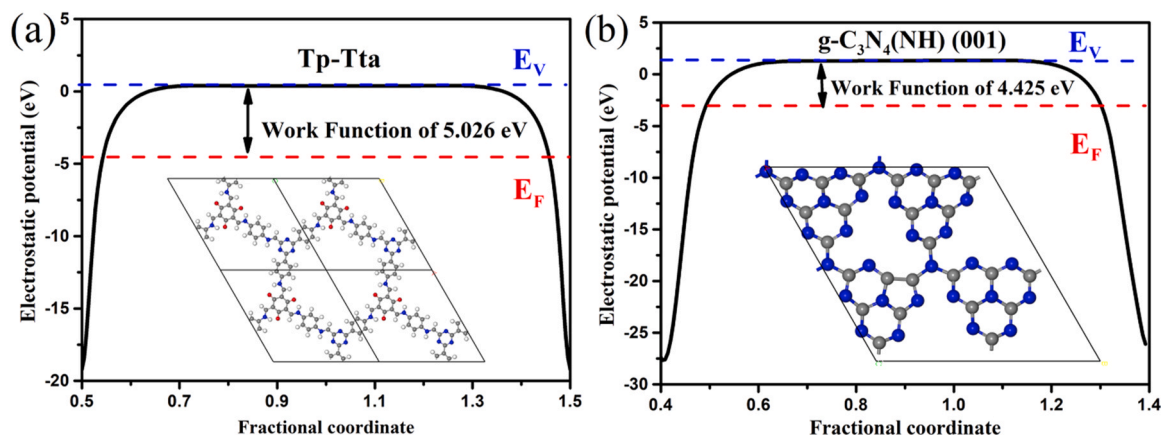


Fig. 3. Electrostatic potentials of Tp-Tta COF (001) (a) and defective C_3N_4 (001) surface (b).

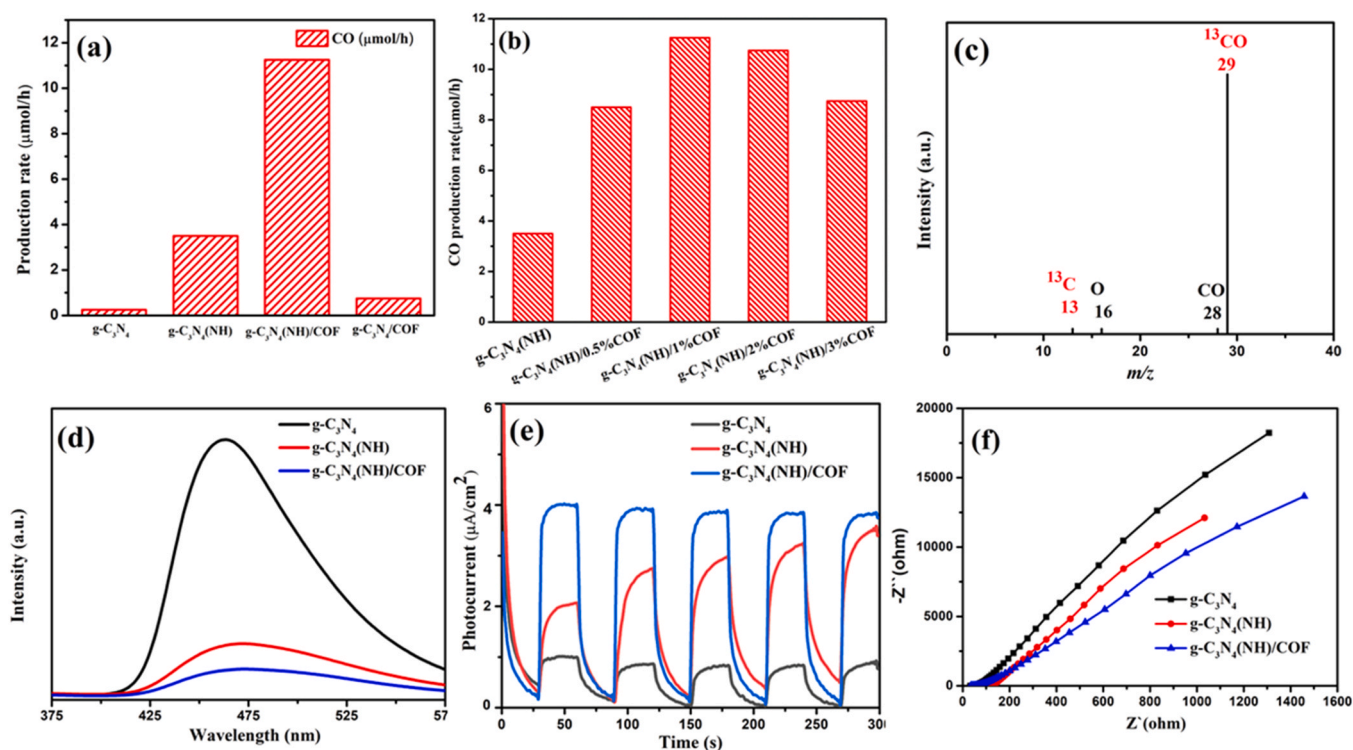


Fig. 4. (a) Photocatalytic CO_2 reduction rate of the prepared samples. (b) Photocatalytic yields of CO for $\text{g-C}_3\text{N}_4(\text{NH})/\text{COF}$ with different amount of COF. (c) Mass spectra of ^{13}CO and total ion chromatography (inset) over $\text{g-C}_3\text{N}_4(\text{NH})/\text{COF}$ in the photocatalytic reduction of $^{13}\text{CO}_2$. Photoluminescence (d), Transient photocurrent (e), Electrochemical impedance spectroscopy (f) of $\text{g-C}_3\text{N}_4$, $\text{g-C}_3\text{N}_4(\text{NH})$ and $\text{g-C}_3\text{N}_4(\text{NH})/\text{COF}$.

~ 700 nm, which is consistent with the literature report that nitrogen-vacancy defects can improve the light absorption. The Tp-Tta COF nanosheets show light absorption nearly in the entire visible light spectrum. Based on the Tauc plots shown in Fig. s8 and s9, the bandgaps of $\text{g-C}_3\text{N}_4(\text{NH})$ and Tp-Tta COF are determined to be 2.50 and 1.68 eV, respectively. For the $\text{g-C}_3\text{N}_4(\text{NH})/\text{COF}$ hybrid sample, the absorption in visible-light region is clearly enhanced, due to the full spectrum absorption of Tp-Tta COF, which will be beneficial for the photocatalytic process.

Density functional theory calculation was adopted to evaluate the work function, which would be helpful to directly understand the interfacial charge transfer process. The calculated electrostatic potentials of the Tp-Tta COF (001), $\text{g-C}_3\text{N}_4$ (001) and defective C_3N_4 (001) with nitrogen vacancies are shown in Fig. 3 and s10. Obviously, the work function of defective $\text{g-C}_3\text{N}_4$ (4.425) is smaller than that of the Tp-

Tta COF (001) plane (5.026), resulting in the higher Fermi level of defective $\text{g-C}_3\text{N}_4$ than Tp-Tta COF. Upon contact, the difference in Fermi levels will force electrons to transfer from defective $\text{g-C}_3\text{N}_4$ to Tp-Tta COF until an equilibrium Fermi level is achieved, which are consistent with the XPS results [37]. Comparably, larger Fermi level gap between defective $\text{g-C}_3\text{N}_4$ and Tp-Tta COF (0.60) than that of pristine $\text{g-C}_3\text{N}_4$ and Tp-Tta COF (0.37) is obtained, which will guarantee more and rapid charges redistribution at the interfaces of $\text{g-C}_3\text{N}_4(\text{NH})/\text{COF}$. Accordingly, interfacial built-in electric fields are formed, which are expected to be more helpful to the separation of charge carriers for the photocatalytic reaction in $\text{g-C}_3\text{N}_4(\text{NH})/\text{COF}$.

3.2. Activity for CO_2 photoreduction

To explore the effect of nitrogen vacancies and vdW heterojunction

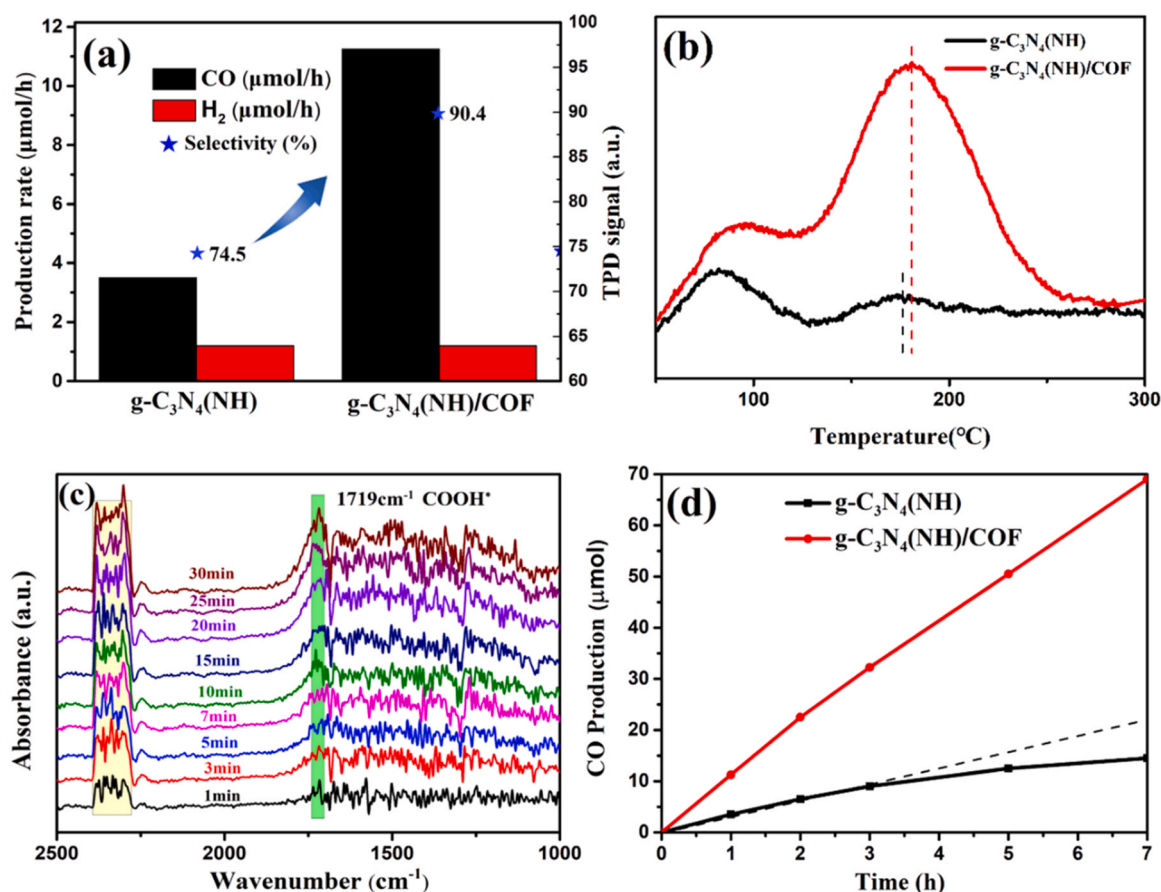


Fig. 5. (a) Photocatalytic yields and selectivity of CO and H₂ for g-C₃N₄ (NH) and g-C₃N₄ (NH)/COF. (b) CO₂-TPD spectra of g-C₃N₄ (NH) and g-C₃N₄ (NH)/COF. (c) In-situ DRIFTS spectra of g-C₃N₄ (NH)/COF obtained under CO₂ gas at different irradiation time. (d) CO production over g-C₃N₄ (NH) and g-C₃N₄ (NH)/COF under 7 h of continuous visible light irradiation.

on the photocatalytic performance, the photoreduction of CO₂ was utilized to evaluate the photocatalytic activity of the prepared samples under visible light irradiation ($\lambda > 400$ nm). As shown in Fig. 4a, the CO yield rate of the pristine g-C₃N₄ is only 0.25 $\mu\text{mol h}^{-1}$, due to the rapid charge recombination. Modification of nitrogen vacancies on g-C₃N₄ can greatly improve the photocatalytic CO₂ reduction performance. As a result, g-C₃N₄ (NH) (3.5 $\mu\text{mol h}^{-1}$) exhibits 14 times higher CO evolution rate than that of pristine g-C₃N₄. The photocatalytic performance can be further improved after Tp-Tta COF modification, and the optimized g-C₃N₄ (NH)/COF photocatalyst exhibits the highest CO evolution rate of 11.25 $\mu\text{mol h}^{-1}$, which is 45 and 3.2 times of g-C₃N₄ and g-C₃N₄ (NH), respectively. By contrast, the performance of g-C₃N₄/COF shows only 0.75 $\mu\text{mol h}^{-1}$ CO evolution rate under the same condition, clearly evincing the synergistic effects of the nitrogen vacancies and heterojunction for enhanced charge separation and transfer ability. To further study the improvement of photocatalytic activity with the hybridizing of Tp-Tta COF into the hybrid, a series of photocatalysts with different weight ratio of COF were investigated. As shown in Fig. 4b, the photocatalytic activity of g-C₃N₄ (NH)/COF materials first increases and then declines as the weight ratio of Tp-Tta COF increased due to the light shielding effect. Specifically, g-C₃N₄ (NH)/1% COF with optimal amount of Tp-Tta COF shows the highest CO evolution rate (11.25 $\mu\text{mol h}^{-1}$), which is comparable to the state-of-the-art heterogeneous photocatalysts for CO₂ reduction (Table S1). In order to certify the carbon source originating from the photocatalytic CO₂ reduction process, isotope-labeled ¹³CO₂ was employed as source gas during the similar photocatalytic reaction. The obtained products were examined by gas chromatography-mass spectrometry (GC-MS). As shown in Fig. 4c, the chromatographic peak appears at 5:19 min is assigned to the generated

¹³CO based on the value of $m/z = 29$ in mass spectrum [38]. This result clearly confirms that the generated CO indeed originates from the photoreduction of CO₂ over g-C₃N₄ (NH)/COF.

Efficient separation and transfer of photogenerated charge carriers is the prerequisite for developing high-activity photocatalyst. To clarify the excellent photocatalytic activity of g-C₃N₄ (NH)/COF, photoluminescence (PL) spectroscopy was conducted to study the photoinduced charge separation. As shown in Fig. 4d, the g-C₃N₄ (NH) shows weaker PL intensity than g-C₃N₄. After being composited with Tp-Tta COF, the PL of g-C₃N₄ (NH)/COF almost completely quenches compared to that of g-C₃N₄ (NH). The results prove that the formed heterojunction can effectively enhance the separation efficiency of charge carriers and thereby optimize the in-plane electron transfer. Transient photocurrent and EIS tests were further applied to measure the charge transfer efficiency. As shown in Fig. 4e, the transient photocurrent response of g-C₃N₄ (NH)/COF is almost 4.7 times and 1.6 times higher than that of g-C₃N₄ and g-C₃N₄ (NH), suggesting that the close linkage and π - π interaction between Tp-Tta COF and defective C₃N₄ are favorable for the charge transfer and migration process. The EIS spectra also show a much smaller radius for g-C₃N₄ (NH)/COF compared with g-C₃N₄ (NH) and g-C₃N₄ (Fig. 4f), implying a lower resistance for interfacial charge transfer separation. All of the above results indicate that the coupling Tp-Tta COF onto g-C₃N₄ (NH) to form a vdW heterojunction can not only promote the separation efficiency of photo-generated carriers, but also accelerate the transfer of interfacial charges, thus promoting the photocatalytic reduction of CO₂.

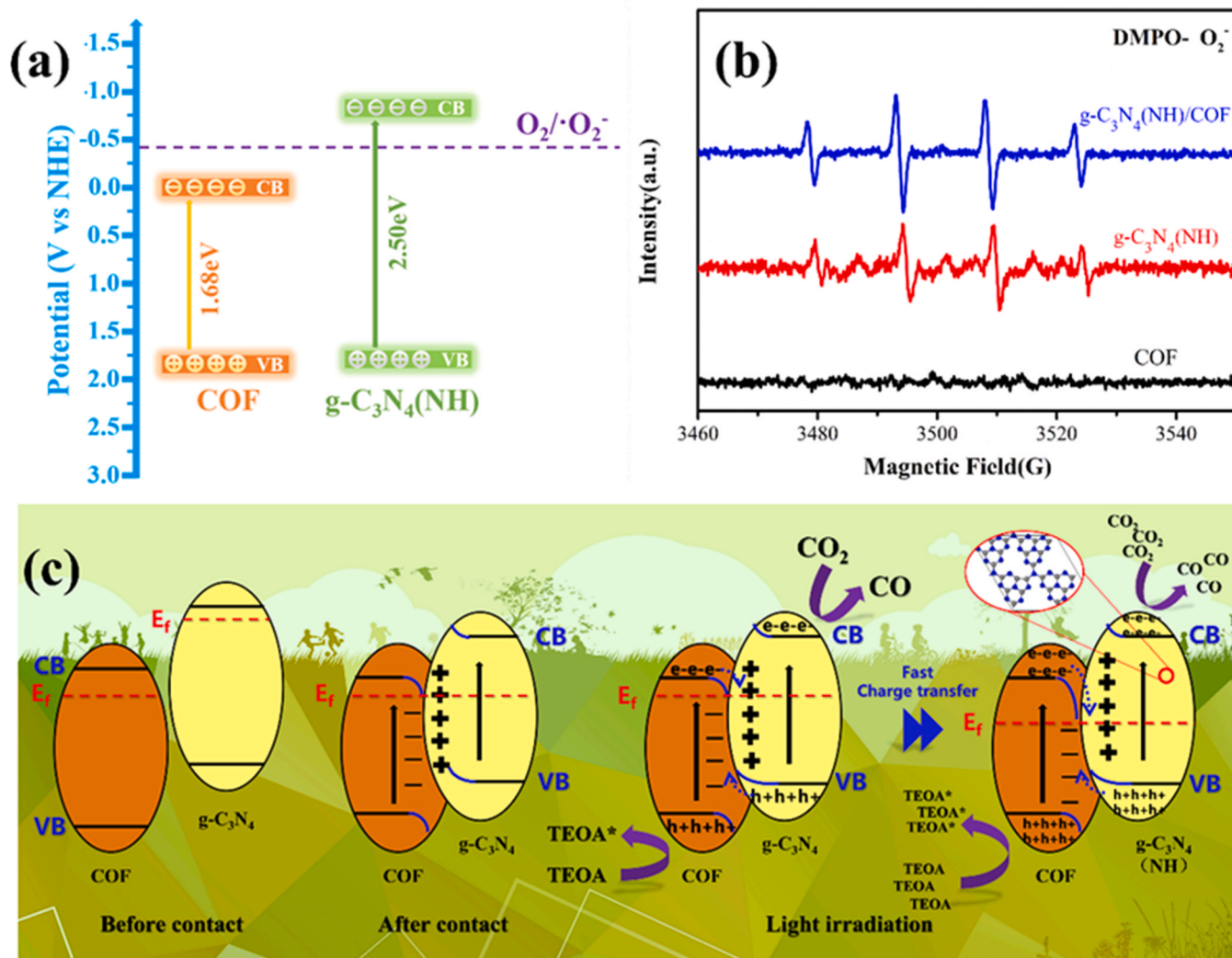


Fig. 6. (a) Band structures g-C₃N₄ (NH) and Tp-Tta COF. (b) EPR spectra of DMPO-•O₂⁻ in an aqueous dispersion of Tp-Tta COF, g-C₃N₄ (NH) and g-C₃N₄ (NH)/COF under irradiation. (c) Schematic illustration of the relative band energy positions and S-scheme charge transfer mechanism between Tp-Tta COF and g-C₃N₄ (NH).

3.3. Selectivity and stability for CO₂ photoreduction

Due to the competitive kinetically favored H₂ generation reaction, the selectivity of photocatalytic reduction of CO₂ is also important to meet the demand of practical applications. According to the results shown in Fig. 5a, the g-C₃N₄ (NH)/COF (90.4%) presents much improved CO selectivity than that of g-C₃N₄ (NH) (74.5%), which demonstrates the promoted CO₂ to CO conversion reaction on g-C₃N₄ (NH)/COF. The temperature-programmed desorption of CO₂ (CO₂-TPD) was carried out to validate the adsorption behavior of CO₂ over different photocatalysts and analysis the structure-activity relationship. As shown in Fig. 5b, the first desorption peak is related to physisorbed CO₂. While, the second peak is associated with chemisorbed CO₂. It is obvious that the CO₂-TPD peak areas for g-C₃N₄ (NH)/COF are much larger than those for g-C₃N₄ (NH), confirming that the coupling of Tp-Tta COF can greatly improve CO₂ adsorption. Besides, the CO₂ desorption peaks of g-C₃N₄ (NH)/COF shift to higher temperature, indicating the stronger interactions between CO₂ and g-C₃N₄ (NH)/COF, which are the prerequisite for the high CO selectivity during photocatalytic reduction reaction [39]. Subsequently, in-situ DRIFTS was used to elucidate the reaction intermediate species and reaction mechanism. As shown in Fig. 5c, the strong broad absorption peak centered at 2339 cm⁻¹ appears during CO₂ photoreduction, which can be ascribed to the absorbed CO₂ molecular. After irradiation, the absorption peak centered at 1719 cm⁻¹

emerges, which is assigned to the asymmetric stretching mode of COOH* intermediate species. Obviously, with extending the irradiation time, the intensity of this peak gradually increases, illustrating the CO₂ reduction over g-C₃N₄ (NH)/COF undergoes the pathway in the order CO₂* → COOH* → CO* and CO [40]. Possessing high activity of g-C₃N₄ (NH)/COF, another key parameter, stability, was investigated. As shown in Fig. 5d, unexpectedly, we note that though g-C₃N₄ (NH) produces considerable amount of CO, after 7 h of continuous visible light irradiation, the rate of CO evolution decreases drastically from 3.5 to 1 μmol h⁻¹. While relatively more stable activity for photocatalytic CO evolution is observed in g-C₃N₄ (NH)/COF, which should be attributed to the accelerated transfer and separation of electron-holes in the g-C₃N₄ (NH)/COF vdW heterostructure containing big π-conjugated aromatic rings.

3.4. Mechanism analysis for CO₂ photoreduction

The band structures of g-C₃N₄ (NH) and Tp-Tta COF were investigated to analyze the photocatalytic mechanism. Firstly, valence band (VB) XPS measurements were conducted to determine the band structure of as-prepared materials (Fig. s11 and s12). The VB position is calculated to be 1.65 and 1.75 eV vs. NHE for g-C₃N₄ (NH) and Tp-Tta COF, respectively. Combined with the band gap from Uv-vis data, the band-structure diagrams of g-C₃N₄ (NH) and Tp-Tta COF are derived and

shown in Fig. 6a. The results show that type-II heterojunction are formed between g-C₃N₄ (NH) and Tp-Tta COF. Secondly, ESR analysis was carried out to determine the interfacial charge transfer process between g-C₃N₄ (NH) and COF. As we know, only the semiconductor with CB potential negative to the redox potential of O₂/•O₂⁻ (−0.33 V vs NHE) can produce •O₂⁻ [41]. Obviously, the CB potentials of g-C₃N₄ (NH) and Tp-Tta COF possess different ability in this process. So, •O₂⁻ was probed using EPR spectra under irradiation on Tp-Tta COF, g-C₃N₄ (NH) and g-C₃N₄ (NH)/COF with DMPO as the trapping agent. As shown in Fig. 6b, no obvious DMPO-•O₂⁻ signal is observed for Tp-Tta COF, which is due to the negligible reduction ability of photogenerated electrons in COF. While, strong DMPO-•O₂⁻ signals are observed for both g-C₃N₄ (NH) and g-C₃N₄ (NH)/COF, suggesting that the photogenerated electrons stay in the CB of g-C₃N₄ (NH). This phenomenon indicates that the charge transfer between g-C₃N₄ (NH) and Tp-Tta COF is contradictory to the conventional type II mechanism. Instead, the S-scheme heterojunction mechanism can fully explain the enhanced CO₂ reduction property of g-C₃N₄ (NH)/COF.

Therefore, combining with the band structure and charge transfer analysis, the mechanism is established and illustrated in Fig. 6c. DFT calculation reveals that the Fermi level of g-C₃N₄ (NH) is higher than that of Tp-Tta COF. Thus, upon contact, the electrons will tend to migrate spontaneously from g-C₃N₄ (NH) to Tp-Tta COF until the Fermi levels reached balance, which are consistent with the XPS results. The charge rearrangement process will result in the bending of band edge and built-in electric field will be established at the interfaces of g-C₃N₄ (NH) and Tp-Tta COF. Under visible light irradiation, both Tp-Tta COF and g-C₃N₄ (NH) will be excited to generate electrons and holes. Under the effect of built-in electric field, electrons in the CB of Tp-Tta COF are prone to recombine with the holes on the VB of g-C₃N₄ (NH) and thus electrons follow the S-scheme path to transfer. The strong interaction between 2D g-C₃N₄ (NH) and Tp-Tta COF is advantageous for the charge transfer and rearrangement of their energy levels, which has been proved by the Mott-Schottky (M-S) plots. As shown in Fig. S13, the plots exhibit positive slopes for both g-C₃N₄ (NH) and Tp-Tta COF, indicating their n-type character and the lower slope of g-C₃N₄ (NH)/COF than that of g-C₃N₄ (NH) and COF indicates the enhanced charge carriers concentration in the vdW heterostructure [42,43]. Moreover, larger Fermi level gap between defective g-C₃N₄ and Tp-Tta COF (0.60) than that of pristine g-C₃N₄ and Tp-Tta COF (0.37) will guarantee more and rapid charges redistribution at the interfaces of g-C₃N₄ (NH)/COF. In addition, the introduction of nitrogen vacancies can improve the light absorption due to its narrow bandgap. Thus, more photoinduced charge carriers will participate in the photoreduction reaction. All these account for the significantly enhanced performance of photocatalytic CO₂ conversion to CO over g-C₃N₄ (NH)/COF.

4. Conclusion

In conclusion, a well-designed g-C₃N₄ (NH)/COF vdW heterostructure with intimate contact interface was constructed for photocatalytic CO₂ reduction reaction. The optimized photocatalytic CO evolution rate for the heterojunction shows 45 and 15 times higher than that of g-C₃N₄ and g-C₃N₄/COF, respectively. More importantly, the π - π stacking interactions leads to the stabilization of the nitrogen vacancies during the reaction. As a result, g-C₃N₄ (NH)/COF exhibits an excellent selectivity and stability in photocatalytic reduction CO₂ to CO. Experimental and theoretical results reveal the superior CO₂ capture, activation and charge deliver features are all integrated in the S-scheme system. This work provides a simple solvent evaporation induced self-assembly strategy to greatly improve the utilization of charge carriers and photocatalytic performance.

CRedit authorship contribution statement

Jiangpeng Wang: Conceptualization, Data curation, Formal

analysis, Methodology, Investigation, Writing – original draft., Yue Yu: Conceptualization, Investigation, Methodology, Validation, Jiayi Cui: Data curation, Validation, Writing – review & editing, Xinran Li: Validation, Yilin Zhang: Visualization, Chao Wang: Validation, Resources, Xuelian Yu: Conceptualization, Methodology, Writing – review & editing, Funding acquisition, Professor Jinhua Ye: Conceptualization, Writing – review & editing, Funding acquisition.

Declaration of Competing Interest

The authors declare that they have no known competing financial interests or personal relationships that could have appeared to influence the work reported in this paper.

Acknowledgements

This work was supported by the Fundamental Research Funds for the Central Universities (2652019031), JSPS KAKENHI (JP18H02065) and the Photo-excitonix Project at Hokkaido University.

Appendix A. Supporting information

Supplementary data associated with this article can be found in the online version at doi:10.1016/j.apcatb.2021.120814.

References

- [1] S.J. Davis, K. Caldeira, H.D. Matthews, Future CO₂ emissions and climate change from existing energy infrastructure, *Science* 329 (2010) 1330–1333, <https://doi.org/10.1126/science.1188566>.
- [2] T. Wigley, The climate change commitment, *Science* 307 (2005) 1766–1769, <https://doi.org/10.1126/science.1103934>.
- [3] Y. Zhang, B. Xia, J. Ran, K. Davey, S.Z. Qiao, Atomic-level reactive sites for semiconductor-based photocatalytic CO₂ reduction, *Adv. Energy Mater.* 10 (2020), 1903879, <https://doi.org/10.1002/aenm.201903879>.
- [4] J.R. Ran, M. Jaroniec, S.Z. Qiao, Cocatalysts in semiconductor-based photocatalytic CO₂ reduction: achievements, challenges, and opportunities, *Adv. Mater.* 30 (2018), 17046449, <https://doi.org/10.1002/adma.201704649>.
- [5] L. Liang, X. Li, Y. Sun, Y. Tan, X. Jiao, H. Ju, Z. Qi, J. Zhu, Infrared light-driven CO₂ overall splitting at room temperature, *Joule* 2 (2018) 1004–1016, <https://doi.org/10.1016/j.joule.2018.02.019>.
- [6] B.R. Sutherland, Charging up stationary energy storage, *Joule* 3 (2019) 1–3, <https://doi.org/10.1016/j.joule.2018.12.022>.
- [7] F. Xu, K. Meng, B. Cheng, S. Wang, J. Yu, Unique S-scheme heterojunctions in self-assembled TiO₂/CsPbBr₃ hybrids for CO₂ photoreduction, *Nat. Commun.* 11 (2020) 4613, <https://doi.org/10.1038/s41467-020-18350-7>.
- [8] J. Li, B. Huang, Q. Guo, S. Guo, B. Liu, Van der Waals heterojunction for selective visible-light-driven photocatalytic CO₂ reduction, *Appl. Catal. B: Environ.* 284 (2021), 119733, <https://doi.org/10.1016/j.apcatb.2020.119733>.
- [9] Y. Jiang, H.-Y. Chen, J.-Y. Li, J.-F. Liao, H.-H. Zhang, X.-D. Wang, D.-B. Kuang, Z-Scheme 2D/2D heterojunction of CsPbBr₃/Bi₂WO₆ for improved photocatalytic CO₂ reduction, *Adv. Funct. Mater.* 30 (2020), 2004293, <https://doi.org/10.1002/adfm.202004293>.
- [10] T. Kong, J. Low, Catalyst: how material chemistry enables solar-driven CO₂ conversion, *Chem* 6 (2020) 1035–1038, <https://doi.org/10.1016/j.chempr.2020.02.014>.
- [11] C. Tan, J. Chen, X.-J. Wu, H. Zhang, Epitaxial growth of hybrid nanostructures, *Nat. Rev. Mater.* 3 (2018) 17089, <https://doi.org/10.1038/natrevmats.2017.89>.
- [12] J. Ran, W. Guo, H. Wang, B. Zhu, J. Yu, S.Z. Qiao, Metal-free 2D/2D phosphorene/g-C₃N₄ Van der Waals heterojunction for highly enhanced visible-light photocatalytic H₂ production, *Adv. Mater.* 30 (2018), 1800128, <https://doi.org/10.1002/adma.201800128>.
- [13] C. Yang, Z. Xue, J. Qin, M. Sawangphruk, X. Zhang, R. Liu, Heterogeneous structural defects to prompt charge shuttle in g-C₃N₄ plane for boosting visible-light photocatalytic activity, *Appl. Catal. B: Environ.* 259 (2019), 118094, <https://doi.org/10.1016/j.apcatb.2019.118094>.
- [14] Y. Song, Q. Sun, B. Aguila, S. Ma, Covalent organic frameworks: opportunities of covalent organic frameworks for advanced applications, *Adv. Sci.* 6 (2019), 1970011, <https://doi.org/10.1002/advs.201970011>.
- [15] W. Zhong, R. Sa, L. Li, Y. He, L. Li, J. Bi, Z. Zhuang, Y. Yu, Z. Zou, A covalent organic framework bearing single Ni sites as a synergistic photocatalyst for selective photoreduction of CO₂ to CO, *J. Am. Chem. Soc.* 141 (2019) 7615–7621, <https://doi.org/10.1021/jacs.9b02997>.
- [16] Z. Fu, X. Wang, A.M. Gardner, X. Wang, S.Y. Chong, G. Neri, A.J. Cowan, L. Liu, X. Li, A. Vogel, R. Clowes, M. Bilton, L. Chen, R.S. Sprick, A.I. Cooper, A stable covalent organic framework for photocatalytic carbon dioxide reduction, *Chem. Sci.* 11 (2020) 543–550, <https://doi.org/10.1039/C9SC03800K>.

- [17] T. Su, Q. Shao, Z. Qin, Z. Guo, Role of Interfaces in two-dimensional photocatalyst for water splitting, 2253–227, ACS Catal. 8 (2018) 2253–2276, <https://doi.org/10.1021/acscatal.7b03437>.
- [18] J. Fu, Q. Xu, J. Low, C. Jiang, J. Yu, Ultrathin 2D/2D WO₃/g-C₃N₄ step-scheme H₂-production photocatalyst, Appl. Catal. B: Environ. 243 (2019) 556–565, <https://doi.org/10.1016/j.apcatb.2018.11.011>.
- [19] Z. Wang, Y. Chen, L. Zhang, B. Cheng, J. Yu, J. Fan, Step-scheme CdS/TiO₂ nanocomposite hollow microsphere with enhanced photocatalytic CO₂ reduction activity, J. Mater. Sci. Technol. 56 (2020) 143–150, <https://doi.org/10.1016/j.jmst.2020.02.062>.
- [20] Q. Xu, L. Zhang, B. Cheng, J. Fan, J. Yu, S-scheme heterojunction photocatalyst, Chem 6 (2020) 1543–1559, <https://doi.org/10.1016/j.chempr.2020.06.010>.
- [21] Y. Qin, H. Li, J. Lu, Y. Feng, F. Meng, C. Ma, Y. Yan, M. Meng, Synergy between van der Waals heterojunction and vacancy in ZnIn₂S₄/g-C₃N₄ 2D/2D photocatalysts for enhanced photocatalytic hydrogen evolution, Appl. Catal. B: Environ. 277 (2020), 119254, <https://doi.org/10.1016/j.apcatb.2020.119254>.
- [22] X. Song, Y. Wu, X. Zhang, X. Li, Z. Zhu, C. Ma, Y. Yan, P. Huo, G. Yang, Boosting charge carriers separation and migration efficiency via fabricating all organic Van der Waals heterojunction for efficient photoreduction of CO₂, Chem. Eng. J. 408 (2021), 127292, <https://doi.org/10.1016/j.cej.2020.127292>.
- [23] Q. Han, B. Wang, J. Gao, Z. Cheng, Y. Zhao, Z. Zhang, L. Qu, Atomically thin mesoporous nanomesh of graphitic C₃N₄ for high-efficiency photocatalytic hydrogen evolution, ACS Nano 10 (2016) 2745–2751, <https://doi.org/10.1021/acsnano.5b07831>.
- [24] Q. Tay, P. Kanhere, C.F. Ng, S. Chen, S. Chakraborty, A.C.H. Huan, T.C. Sum, R. Ahuja, Z. Chen, Defect engineered g-C₃N₄ for efficient visible light photocatalytic hydrogen production, Chem. Mater. 27 (2015) 4930–4933, <http://dx.chinadoc.cn/10.1021/acs.chemmater.5602344>.
- [25] M.D. Segall, P.J.D. Lindan, M.J. Probert, C.J. Pickard, P.J. Hasnip, S.J. Clark, M. C. Payne, First-principles simulation: ideas, illustrations and the CASTEP code, J. Phys. Condens. Matter 14 (2002) 2717–2744, <https://doi.org/10.1088/0953-8984/14/11/301>.
- [26] J.P. Perdew, K. Burke, M. Ernzerhof, Generalized gradient approximation made simple, Phys. Rev. Lett. 77 (1996) 3865–3868, <https://doi.org/10.1103/PhysRevLett.77.3865>.
- [27] D.R. Hamann, M. Schlüter, C. Chiang, Norm-conserving pseudopotentials, Phys. Rev. Lett. 43 (1979) 1494–1497, <https://doi.org/10.1103/PhysRevLett.43.1494>.
- [28] A. Thomas, A. Fischer, F. Goettmann, M. Antonietti, J.-O. Müller, R. Schlögl, J. M. Carlsson, Graphitic carbon nitride materials: variation of structure and morphology and their use as metal-free catalysts, J. Mater. Chem. 18 (2008) 4893–4908, <https://doi.org/10.1039/B800274F>.
- [29] K. Dey, M. Pal, K.C. Rout, S. Kunjattu, H., A. Das, R. Mukherjee, U.K. Kharul, R. Banerjee, Selective molecular separation by interfacially crystallized covalent organic framework thin films, J. Am. Chem. Soc. 139 (2017) 13083–13091, <https://doi.org/10.1021/jacs.7b06640>.
- [30] W. Gao, G. Li, H. Liu, Y. Tian, W.-T. Li, Y. Fa, Y. Cai, Z. Zhao, Y.-L. Yu, G. Qu, G. Jiang, Covalent organic frameworks with tunable pore sizes enhanced solid-phase microextraction direct ionization mass spectrometry for ultrasensitive and rapid analysis of tetrabromo bisphenol A derivatives, Sci. Total Environ. 764 (2021), 144388, <https://doi.org/10.1016/j.scitotenv.2020.144388>.
- [31] Y. Ran, X. Yu, J. Liu, J. Cui, Y. Zhang, X. Xiang, J. Ye, Polymeric carbon nitride with frustrated Lewis pair sites for enhanced photofixation of nitrogen, J. Mater. Chem. A 8 (2020) 13292–13298, <https://doi.org/10.1039/D0TA03914D>.
- [32] M. Luo, Q. Yang, K. Liu, H. Cao, Boosting photocatalytic H₂ evolution on g-C₃N₄ by modifying covalent organic frameworks (COFs), Chem. Commun. 55 (2019) 5829–5832, <https://doi.org/10.1039/C9CC02144B>.
- [33] K. Dey, K.H. Shebeeb, R. Banerjee, Nanoparticle size fractionation through self-standing porous covalent organic framework films, Angew. Chem. Int. Ed. 59 (2020) 1161–1165, <https://doi.org/10.1002/ange.201912381>.
- [34] Y. Yang, Z. Tang, B. Zhou, J. Shen, H. He, A. Ali, Q. Zhong, Y. Xiong, C. Gao, A. Alsaedi, T. Hayat, X. Wang, Y. Zhou, In situ no-slot joint integration of half-metallic C(CN)₃ cocatalyst into g-C₃N₄ scaffold: An absolute metal-free in-plane heterosystem for efficient and selective photoconversion of CO₂ into CO, Appl. Catal. B: Environ. 264 (2020), 118470, <https://doi.org/10.1016/j.apcatb.2019.118470>.
- [35] H. Yu, R. Shi, Y. Zhao, T. Bian, Y. Zhao, C. Zhou, G.I.N. Waterhouse, L.-Z. Wu, C. H. Tung, T. Zhang, Alkali-assisted synthesis of nitrogen deficient graphitic carbon nitride with tunable band structures for efficient visible-light-driven hydrogen evolution, Adv. Mater. 29 (2017), 1605148, <https://doi.org/10.1002/adma.201605148>.
- [36] H. Lan, L. Li, X. An, F. Liu, C. Chen, Microstructure of carbon nitride affecting synergistic photocatalytic activity: hydrogen bonds vs. structural defects, Appl. Catal. B: Environ. 204 (2017) 49–57, <https://doi.org/10.1016/j.apcatb.2016.11.022>.
- [37] J. Liu, Origin of high photocatalytic efficiency in monolayer g-C₃N₄/CdS heterostructure: a hybrid DFT study, J. Phys. Chem. C. 119 (2015) 28417–28423, <https://doi.org/10.1021/acs.jpcc.5b09092>.
- [38] Y. Li, S. Wang, X. Wang, Y. He, Q. Wang, Y. Li, M. Li, G. Yang, J. Yi, H. Lin, D. Huang, L. Li, Facile top-down strategy for direct metal atomization and coordination achieving a high turnover number in CO₂ photoreduction, J. Am. Chem. Soc. 142 (2020) 19259–19267, <https://doi.org/10.1021/jacs.0c09060>.
- [39] Y. He, H. Rao, K. Song, J. Li, Y. Yu, Y. Lou, C. Li, Y. Han, 3D hierarchical ZnIn₂S₄ nanosheets with rich Zn vacancies boosting photocatalytic CO₂ reduction, Adv. Funct. Mater. 29 (2019), 1905153, <https://doi.org/10.1002/adfm.201905153>.
- [40] F. Pan, W. Deng, C. Justiniano, Y. Li, Identification of champion transition metals centers in metal and nitrogen-codoped carbon catalysts for CO₂ reduction, Appl. Catal. B: Environ. 226 (2018) 463–472, <https://doi.org/10.1016/j.apcatb.2018.01.001>.
- [41] A. Meng, B. Cheng, H. Tan, J. Fan, C. Su, J. Yu, TiO₂/polydopamine S-scheme heterojunction photocatalyst with enhanced CO₂-reduction selectivity, Appl. Catal. B: Environ. 289 (2021), 120039, <https://doi.org/10.1016/j.apcatb.2021.120039>.
- [42] M. Zhang, J. Wang, H. Xue, J. Zhang, S. Peng, X. Han, Y. Deng, Acceptor-doping accelerated charge separation in Cu₂O photocathode for photoelectrochemical water splitting: theoretical and experimental studies, Angew. Chem. Int. Ed. 59 (2020) 18463–18467, <https://doi.org/10.1002/anie.202007680>.
- [43] S. Luo, J. Ke, M. Yuan, Q. Zhang, P. Xie, L. Deng, S. Wang, CuInS₂ quantum dots embedded in Bi₂WO₆ nanoflowers for enhanced visible light photocatalytic removal of contaminants, Appl. Catal. B: Environ. 221 (2018) 215–222, <https://doi.org/10.1016/j.apcatb.2017.09.028>.